Microplasticity in Polycrystals: A Thermomechanical Experimental Perspective

Eric Charkaluk, Rian Seghir, Laurence Bodelot, Jean-Francois Witz, Philippe Dufrenoy

Microplasticity in Polycrystals: A Thermomechanical Experimental Perspective

E. Charkaluk · R. Seghir · L. Bodelot · J.-F. Witz · P. Dufrénoy

Abstract In this paper, thermomechanical couplings at the grain scale in metallic polycrystals are studied during the deformation process through an original experimental setup and improved calibration tools and full-field treatments. In order to perform intragranular thermomechanical analysis in a metallic polycrystal at the grain scale, a crystallography-based technique for the projection of the temperature and displacement fields on a polynomial basis is proposed. It enables intragranular coupled analysis of strain and temperature full-field data. Macroscopic, mesoscopic and granular analysis are then conducted and it is shown that the determination of a macroscopic yield stress as well as a critical resolved shear stress in grains is possible. Early local microplastic activity is therefore thermomechanically confirmed.

Keywords Infrared thermography · Digital image correlation · Microstructure · EBSD · Plasticity

Introduction

During the mechanical loading of metallic polycrystals, the diversity of grain orientations leads to inhomogeneous deformation and results in local plasticity. These aspects have been studied and modeled for many decades and one can cite, for example, the pioneering works of [1, 2] and [3]. These observations are extensively described, synthesized and modeled in the Cottrell's reference book [4]. The clear observation of an inhomogeneous deformation field in polycrystals has been particularly emphasized by [5] and [6]. As microplasticity occurs progressively in metallic materials, the definition and the determination of a plastic yield stress is not a trivial task. An interesting historical perspective on this subject is given in [7] through kinematic and stenic analysis. Though, many empirical methods have been proposed. However, the estimation of a yield stress corresponding to the first plastic activity in a polycrystal is still a considerable challenge. Following the pioneering work of [8], an alternative way is the analysis of the thermal effects induced by a mechanical loading through thermomechanical coupling. In fact, during deformation, this local and then global plasticity triggers a dissipation thus a temperature increase in the specimen, a phenomenon that was studied very early by Taylor and co-workers [8–10] using global calorimetric measurements. [11] then proposed a temperature-based method for the determination of a yield stress which was defined at the transition between thermoelastic and thermoelastoplastic regimes.

Moreover, it is also well-known that most of the plastic work reappears in the form of heat whereas during cold-working, a certain proportion of this plastic work, often named stored energy, remains latent in the material and is associated with microstructure changes, including mainly dislocation elastic energy. An extensive review of the early work within this field was published by [12] who defined more precisely the energy balance concept as the estimation of the dissipated and stored part of the mechanical energy given to the material. Since the late 80's, many attempts have been made to access such energy balances

E. Charkaluk (✉) · R. Seghir · J.-F. Witz · P. Dufrénoy
Laboratoire de Mécanique de Lille, CNRS UMR 8107,
F-59655 Villeneuve d'Ascq, France
e-mail: eric.charkaluk@ec-lille.fr

L. Bodelot
Laboratoire de Mécanique des Solides, CNRS UMR 7649,
F-91128 Palaiseau, France

using infrared radiometers or cameras [13–16] so as to move from global to full-field measurements. Since it has been shown that the material class and the microstructure have notable effects on the energy balance [17, 18], an estimation at the grain scale also becomes an interesting challenge in order to propose thermodynamic based crystal plasticity models.

However, as quasi-static deformation processes lead to very low temperature variations that occur at a very local scale, making any experimental estimation of plastic activity and stored energy at the grain scale is laborious and complicated. As a result, to date, very few authors have attempted such a thermomechanical analysis at the microstructure scale of a polycrystal using coupled full-field measurements combined with the heat equation. Only preliminary steps were carried out on oligocrystals ($<$ 10 grains) [19, 20]. To our knowledge, the first attempt on polycrystals (hundreds or thousands of grains) based on a kinematic full-field measurement combined with a thermal measurement can be attributed to Bodelot et al. [21] who used an original experimental device [22] on a quenched A316L austenitic stainless steel at a low strain level (i.e., $<$ 10 %) under quasi-static monotonic tensile loading. The first objective of this paper is to present the original tools developed for the study of thermomechanical couplings in polycrystals. The second objective is to use those tools to conduct global and then local analysis during the deformation process, which will be focused in the present case on macro- and microplasticity phenomena.

After this introduction, the paper is divided into four parts. In the first one, the main characteristics of the experimental data of Bodelot et al. [22] are summarized. In the second part, the calibration procedure and the crystallography-based technique for the projection of these initial data onto the microstructure using a polynomial basis are described. The thermomechanical fields obtained for the whole surface microstructure are then discussed. Finally, in the third part, granular analysis are proposed and show the pertinence of such data processing through the determination of a macroscopic yield stress and of a Critical Resolved Shear Stress (CRSS).

Experimental Data

Test and Material

The material studied is an AISI 316L austenitic stainless steel. Dog-bone shaped flat samples, 2 mm thick, were heat-treated under air for 2 h at 1,200°C and immediately water-quenched. A displacement-controlled monotonic tensile test was applied to the sample with a constant strain rate of $5.10^{-3}\ s^{-1}$ [21].

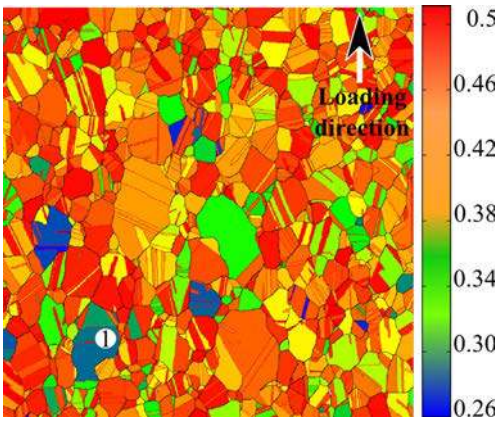

Fig. 1 Maximum Schmid factor relative to the loading direction of each grain of the 5 mm × 5 mm zone of interest

Electron Back-Scattered Diffraction (EBSD) analysis was conducted within a Jeol 6100 scanning electron microscope with a conventional electron gun operating at 25kV; the probe current was on the order of 1 nA. Analyses were performed with OIM software provided by TSL with a pitch of 20 μm. The EBSD analysis shows that, in the 5 mm × 5 mm central area of interest, the microstructure is composed of 1,776 grains with a 118μm mean grain size, calculated from the EBSD analysis, based on the equivalent circle diameter method. One can already underline that grain size is clearly heterogeneous, from millimetric grains to very small ones. Figure 1 presents the maximum Schmid factor computed for the loading direction. It shows that the mean maximum Schmid factor is 0.44 and evidences that the major part of the studied area exhibits a maximum Schmid factor higher than 0.45 even if some grains exhibit very low values, notably in the region denoted 1. One has also to observe on this EBSD analysis that many small grains, more particularly in the central axis of the specimen, possess the lowest Schmid factor.

Figure 2 shows the grain boundary pattern. Black lines show High Angle Grain Boundaries ($HAGBs$), i.e where the misorientation ranges from $\approx$ 10^o to 180^o whereas red ones show twin boundaries (Σ_3), i.e where lattices are related by a 60^o rotation about the $\langle 111 \rangle$ crystal direction, classically denoted by $\langle 111 \rangle \langle 60^o \rangle$. In the present case, the occurrence of Σ_3 interfaces is significant, due to the initial heat treatment. Here, 57 % of grain boundaries are Σ_3 ones[1]. One can also note that, if one does not consider Σ_3 boundaries, the mean grain size increases from 118 μm to 237 μm with a quasi perfect equiaxed shape (equiaxiality ratio = 0.51).

Figure 3 presents a micrography of the 5 mm × 5 mm central area after the test. One can distinguish zones

[1] HAGBs total length in the central area = 62.86 cm - Σ_3 GBs length = 36.36 cm

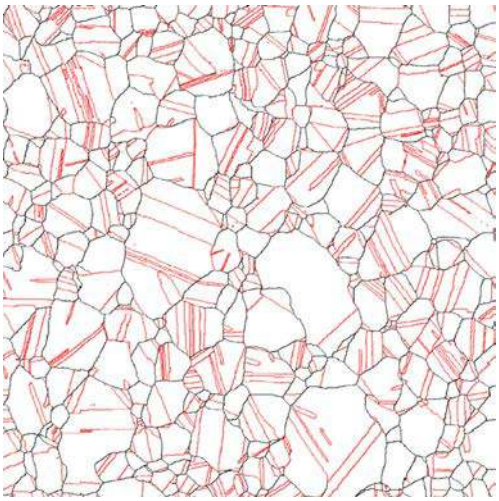

Fig. 2 Grain boundary network in the 5 mm × 5 mm zone of interest (in black: High Angle Grain Boundaries, in red: Σ3-type twin boundaries)

with many slip bands corresponding to a high intragranular plastic activity during the tensile loading and other zones located at the grain or twin boundaries, that exhibit large discontinuities in terms of boundaries relative motions.

In order to obtain information about these microstructural out-of-plane displacements, the topography of the specimen surface has been measured after the test. This profilometric analysis has been performed on a Wyko NT 9300 (Veeco) interferometric profilometer with a $5\mu m$ lateral step. The specimen surface was originally polished up to $1\mu m$ diamond finish and the vertical resolution is 3nm. Hence the observed topography that exhibits values largely above these numbers can be attributed to the mechanisms that arose during the loading of the sample. These out-of plane displacements result from a combination of out-of-plane rigid body motion and out-of-plane plastic strains induced by the constraints that grains experience at their boundaries.

In Fig. 4, the grain boundaries are superimposed onto the above-mentioned profilometric analysis. One observes that the relief ranges from -12μm to 11μm. Consequently the specimen gauge surface evolved from an initial variation of topography close to $1\mu m$ to more than $20\mu m$ during the tensile test. It reflects an important plastic activity of the free surface. If one considers the mean value $\approx$ 0 as the reference, the field exhibits some large domains (surrounded by thick black lines in Fig. 4) "plunging inside" the material whereas the rest of specimen have emerged from the surface. As shown in Fig. 4, this field emphasizes a concrete link between the grain boundary pattern and the surface topography. Indeed, out-of-plane displacement discontinuities seems to be widely connected to grain boundary network and reach $10\mu m$ in some areas.

Fully-Coupled Measurements of Kinematic and Thermal Fields

Complementary to these microstructural investigations, an original experimental setup was proposed. It is able to measure, in the same location and at the same time, kinematic and thermal fields at the microstructural scale of flat samples during mechanical tests. The main features are described in [22] and some improvements in the data processing have been developed in [23].

Strain fields are obtained using Digital Image Correlation (DIC) performed with $Correli\,Q^4$ [24] on images of the deforming sample covered with a speckle pattern taken with a CCD camera. The precision on displacement values is $4.10^{-2}\mu m$ for a resolution of 104 μm × 104 μm

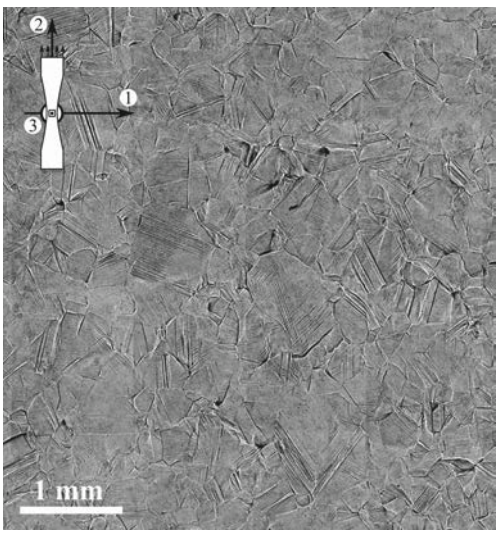

Fig. 3 Micrography of the 5 mm × 5 mm central area after the test with the specimen frame orientations

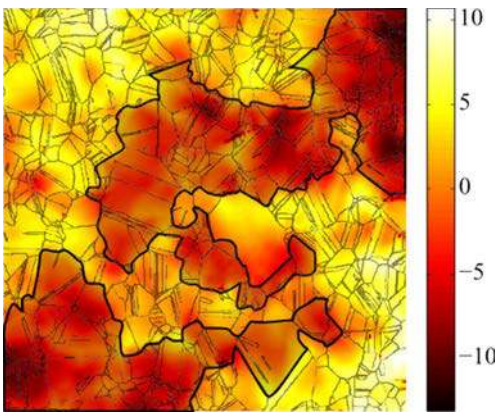

Fig. 4 Profilometric analysis of the out-of-plane displacement field (in μm) obtained after the test in the 5 mm × 5 mm central area

and the recording frequency is 7 Hz. Temperature fields are obtained by Infrared Thermography (IRT) with a resulting frequency of 25Hz and a spatial resolution of 90 μm $\times$ 90 μm for the thermal fields. This resolution limit corresponds to a 3 $\times$ 3 reference subset of 30 μm $\times$ 30 μm pixels as recommended in [25] and leads to a thermal precision of 30 mK [23]. Thus, the mean grain size of the tested sample (see "Test and Material") matches the spatial resolution capabilities of both measurement techniques. According to individual grain size analysis, more than 84 % of the zone of interest is suitable for granular full-field measurements analysis. More particularly, approximatively 20 grains possess a grain size greater than 400 μm, which largely enables an intragranular investigation.

Since the microstructure of a polycrystal is generally different from one face to the other on a flat specimen, the same area of the sample has to be observed simultaneously by both CCD and IRT cameras. To achieve such a fully-coupled observation of the same zone, a dichroic mirror was placed in front of the sample, making a 45^o angle with the normal to its surface (see Fig. 5 and [22]). Given its filtering properties, the dichroic mirror transmits the infrared radiation towards the infrared camera located in front of the sample and reflects the rest of the radiation, including the visible radiation, towards the CCD camera which is perpendicular to the normal of the sample. To achieve coupled measurements, a special coating made of micron-scale metal oxides powder was designed and applied on the sample, simultaneously meeting the requirements of both measurement techniques with the magnifications used. Indeed, this coating made has a high emissivity thanks to the micron-scale roughness of the powder and exhibits a wide range of gray levels at the micron scale thanks to the mixing of several oxides. Finally, the DIC displacement data allowed tracking the displacement of material points in front of the infrared array and then expressing the thermal fields in the undeformed configuration. Therefore, the data is fully coupled insofar as both fields correspond to the same zone at the same time and are given in the undeformed configuration.

Thermal Calibration and Numerical Projection of Fields on Grains

Calibration

In addition to this experimental imaging systems coupling setup, recovering an accurate in-situ thermal field on the specimen surface requires a specific calibration strategy described in particular in [22, 26] and extended to the present case by [23]. Only the main features will be described in this section.

Some constraints have to be taken into account. First, the IR-camera does not measure temperature but radiative flux and does not express it in physical units but in Digital Level (or gray level). Next, the measurements could be affected by optical distortions and each sensor of the IRFPA camera has its own dynamics and noise. Thirdly, the relationship between radiative flux and temperature depends on the surface and volume properties of the specimen such as emissivity, diffusivity, ... Finally, external heat sources could dramatically affect the observed thermal scene.

To solve the first three constraints, a pixel-to-pixel [26] "flux calibration" with an extended blackbody set at different reference temperatures is implemented in the same experimental conditions. The pixel-to-pixel strategy takes advantage of each IRT sensor dynamics contrary to the classical two-point Non Uniformity Correction (NUC), thus improving the spatial acuteness. Moreover, the flux-based calibration allows considering the effective emissivity of the reference blackbody and the one of the tested specimen.

The last problem of emissivity variation, especially due to the heterogeneity of the coating used for DIC and the potential external heat sources, is solved considering the following assumption: reflections and "apparent emissivity" affect the observed field at different spatial scales and are not attached to the same reference system. Indeed, reflections could be considered as a low spatial frequency and Eulerian phenomena (reflection spots do not move when the specimen is stretched), contrary to emissivity or diffusivity variations which affect the infrared field at high spatial frequency (characteristic size of coating heterogeneities)

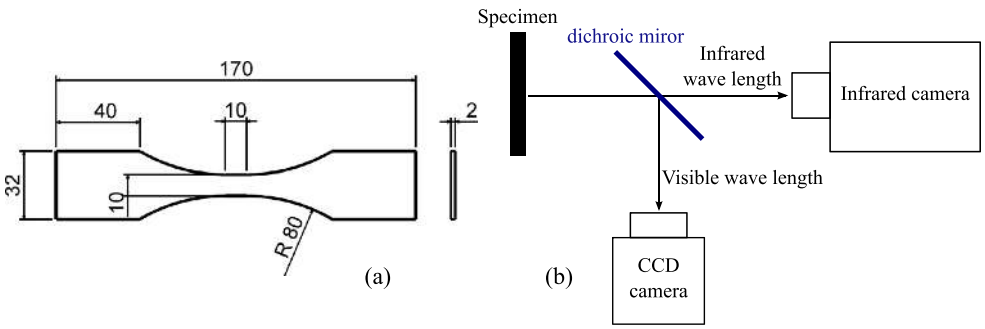

Fig. 5 Specimen geometry and schematic representation of the experimental setup proposed in [22]

and which are Lagrangian (the "apparent emissivity" field moves and deforms with the specimen).

Considering a test period when the specimen is in a thermal equilibrium, i.e not loaded yet, a Fourier decomposition of the measured flux in Low and High Spatial Frequencies (LSF and HSF) conducts to the estimation of these different parts of the signal, as described by equations (1) and (2):

$$\phi_{refl} = \phi|_{LSF} - \bar{\epsilon}_{obj}\sigma\bar{T}^4_{obj} + \sigma T^4_{cam} \tag{1}$$

$$\epsilon_{obj} = \frac{\phi - \left(\phi|_{LSF} - \bar{\epsilon}_{obj}\sigma\bar{T}^4_{obj}\right)}{\sigma\bar{T}^4_{obj}} \tag{2}$$

where ϕ is the measured radiative flux, $\phi|_{LSF}$ is its LSF part obtained by Fourier decomposition. $\bar{\epsilon}_{obj}$, $\bar{T}_{obj}$ are the mean surface emissivity and temperature respectively [22], T_{cam} is the temperature of the IRT sensor cooled at $77K$ and σ the Boltzmann constant, $\sigma = 5.67032\text{x}10^{-8}\ Wm^{-2}K^{-4}$. Figure 6 presents the flux decomposition over the specimen surface.

Finally, the "apparent emissivity" field determined from the Fourier decomposition is applied to the whole infrared scene, previously calibrated and expressed in the undeformed configuration. It allows recovering a thermal image sequence of the specimen surface during the deformation process, taking into account previously described local and global experimental bias.

Fields Projection on the Microctructure

Now, to reach our goal of conducting cristallography-based investigations, we propose to use the complementary EBSD field in order to project the initial measurements onto the microstructure [27]. In fact, the only piece of EBSD data used here is the boundary network within the central area

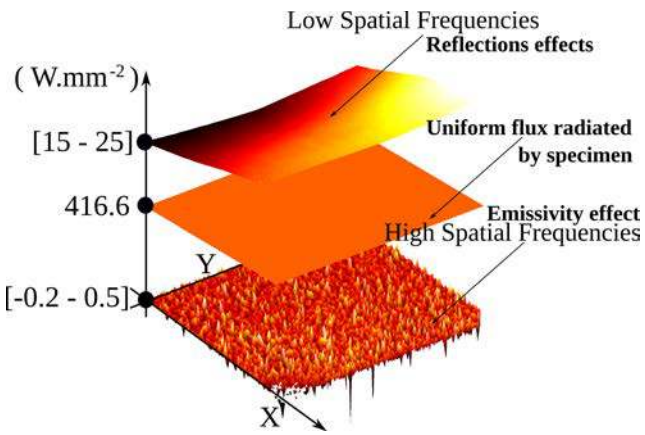

Fig. 6 flux decomposition in low spatial frequencies (LSF), high spatial ones (HSF), and uniform ones

analyzed, the crystallographic orientations are not taken into account for the projection. The grain (or twin) boundary network constitutes a natural partition between intra- and intergranular domains and it is well known that grain and twin boundaries highly participate to the deformation accommodation processes [28]. This aspect is supported by the profilometric analysis described in the previous section. By comparing this field to the microstructure, a more precise analysis shows that the largest displacement gradients are located around grain and twin boundaries where high strain incompatibilities are observed after the test. Consequently, it appears unjustified to smooth the displacement field over grain boundaries as obtained by a classical DIC technique. Here, no thermal and kinematic continuities will be imposed at grain boundaries as they represent a natural discontinuity network within the polycrystal: kinematic and thermal continuities are not ensured through these boundaries. For displacements, this is supported by the profilometric analysis (see Fig. 4) and for temperature, this is justified by studies on the Kapitza effect [29]. Therefore, taking into account grain boundary discontinuities, the proposed treatment leads to the definition of a projection domain in which the interpolated functions fit the whole set of intragranular experimental data. Then the grain-based projection intrinsically leads to discontinuities at grain boundaries, but one has to underline that these are not measurements of these discontinuities. Moreover, intragranular quantities can be differentiated in a simple analytical way.

This projection operation requires selecting a granular projection basis. This choice is based on different elements: (1) the ability to render the global shape of the observed fields with each grain, (2) its ease of implementation within a least-squares minimization, i.e., a problem with separable variables. In this context, simple polynomial functions are assumed:

$$A^g = (A_0 \quad A_1 \quad A_2 \quad \dots \quad A_m) \tag{3}$$

$$N = \left(1 \quad X \quad Y \quad X^2 \quad Y^2 \quad XY \quad \dots \quad X_m\right) \tag{4}$$

$$F^g = \sum_{k=1}^{m} A^g_k \cdot N_k \tag{5}$$

with A^g a set of constants associated within each grain, N the shape function and F the interpolated functions. In order to reach the conclusion that second degree polynomials were the most appropriate choice for the shape functions, we analyzed the discrepancy in terms of residues (level and spatial distribution) between raw-but calibrated-fields and projected fields obtained by polynomials of different orders. Second degree polynomials (only functions of 1, X, Y, XY, X^2 and Y^2 in the present case) appeared to be a good compromise between precision and ease of implementation. The

consequences of this second-order polynomial projection technique are the following:

1. **Biparabolic displacement field**: displacement fields within each grain and at each time increment are projected on a biparabolic basis and, as strain is calculated from the displacement gradient, we implicitly assume here a bilinear strain field within the grain. As many grains of the 5 mm × 5 mm central area exhibit a single slip system activation, this assumption is relatively consistent even if it certainly results in greater errors where multiple slip systems activation is observed. The knowledge of the analytic expression of the in-plane displacement field $\underline{u}(x, y)$ within each grain allows an analytic differentiation and the local estimation of each plane component of the strain tensor, i.e., ε_{11}, ε_{22}, ε_{12} as well as the in-plane component of the spin tensor w_{12}, which can be determined by with $\mathbf{F} = \frac{1}{2}\left(\text{grad}(\underline{u}) + {}^{T}\text{grad}(\underline{u})\right)$, $\varepsilon = \frac{1}{2}\left(\mathbf{F} + {}^{T}\mathbf{F}\right)$ and $\mathbf{w} = \frac{1}{2}\left(\mathbf{F} - {}^{T}\mathbf{F}\right)$.
2. **Biparabolic thermal field**: as conductive fluxes are calculated from the temperature Laplacian, uniform conductive exchanges within the grain at each instant are implicitly assumed through this hypothesis. As every local heat source initiated within the grain is quickly uniform due to the conductive phenomenon, it is therefore assumed that conductive exchanges are instantaneously uniform within the grain and on its boundaries. Then, as for displacement fields, the thermal field can be analytically differentiated. As the improvement of intragranular accuracy, when considering averages within grains, is clearly depending of the grain size, it is difficult to define an accuracy map but the value of 30 mK remains a lower bound as it can be observed in the following results.

It should be pointed out that no data is lost in this projection procedure. Indeed, the whole decomposition is additive, while residual fields between initial fields and the projected field are complementary and can be separately analyzed. One has to underline that the projection method globally decrease the systematic error and its standard deviation. However, in the case of grains with a size lower than the spatial IRT and DIC resolutions, fields are projected on lower order polynomial functions. Indeed, for grains which contains few than 12 (20 μm × 20μm) pixels the projection basis is reduced to the following linear one (1, X, Y). Thus, this projection on lower order polynomial induces a more important error in these area. But, one could recall that more than 84 % of the studied area contains grains whose size is greater than the spatial IRT and DIC resolutions. Therefore, the present study will focus on the biggest grains. Finally, in order to determine the polynomial parameters set for the entire analyzed zone, a least-squares method is used and is solved in all the grains of the central 5 mm x 5mm area and at each time increment. All the corresponding details are presented in [27].

Thermomechanical Fields Analysis

Macroscopic Mean Values and Yield Stress Definition

One introduces first thermomechanical results from a macroscopic and mesoscopic point of view, i.e. results presented in this section are spatial mean quantities estimated over the surface gauge-section (5 mm x 5mm) of the specimen; it reflects therefore the mean thermomechanical response of 1,776 surface grains and the associated in-depth grains. These mean values will be confronted in the next section to the evolution of the thermomechanical full-fields. Figure 7 presents the stress-strain curve as well as the temperature-strain curve during the whole test.

On a stress-strain curve, one classically plots a 0.2 % offset in order to define the plastic yield stress (which is equal here to 223 MPa) as shown in Fig. 7, even if plasticity begins before this conventional point. However, a precise determination of the initial yield stress is always a difficult and subjective task, when only based on stress-strain values consideration (see for example the interesting paper of [7]).

In this way, following [11], one can also consider here the mean relative thermal evolution, i.e. $\theta = T - T_0$ where T is the absolute current temperature and T_0 the initial one, presented in Fig. 7. One observes a first drop in temperature between instants A and B', both located in the conventional elastic domain, followed by a rise between

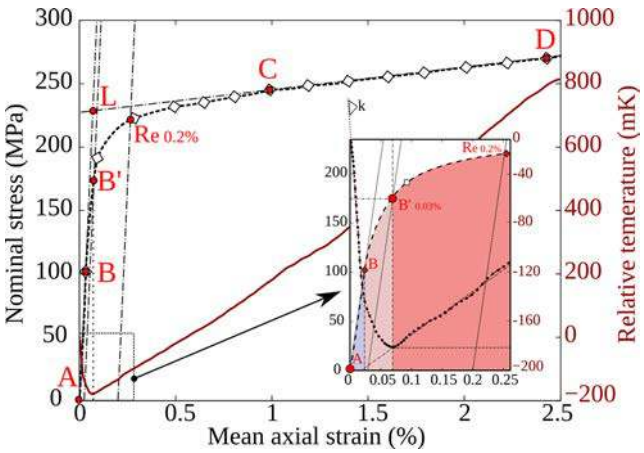

Fig. 7 Mean stress-strain (*in dotted black*) and temperature-strain (*in red*) evolutions averaged over the specimen gauge-section (5 mm x 5mm)

instants B' and D. Thermodynamically, these thermal evolutions are respectively associated with the thermoelastic coupling (which implies a thermal drop in tension and a rise in compression) and then with the plastic dissipation. More precisely, if one considers linear thermoelasticity, the thermal evolution has to be linear until the first occurrence of dissipative plastic phenomena. Therefore, it is interesting to note that the deviation from linearity point in the thermal curve occurs actually at point B. Thus this point corresponds thermally to the beginning of a deviation from purely linear elastic behavior i.e. to the first occurrence of dissipative phenomena. This dissipation is then sufficiently important at point B' so that a minimum thermal value is attained and so that the temperature begins increasing continuously.

For the tested specimen (see Fig. 7), the thermal loss of linearity appears at 106 MPa and the minimum temperature, -180 mK, is reached at 172 MPa of nominal stress. Both values, 106 and 172 MPa of nominal stress, correspond respectively to $\approx$ 0 % and $\approx$ 0.03 % of residual plastic strain. The analysis of the temperature evolution is therefore convenient to define a plastic yield stress precisely. Note that the value of $\approx$ 0.03 % of residual plastic strain when the temperature increases again is also reported in [11] for a large class of metallic materials.

It is now interesting to consider the thermomechanical fields in order to relate the stress-strain curve to strain and temperature spatial distributions.

Stain and Temperature Heterogeneity and Microplasticity

In this section, strain fields, obtained by analytic intragranular diffrentiation of the projected displacement fields (see previous sections and also [27]), as well as thermal fields, are presented at different stages. One has to note that he following figures are plotted in the deformed configuration to emphasize the largely more pronounced deformation state in the plastic regime.

Figure 8 presents the axial strain fields at the point (B) and during the plastic regime (C). In both cases, one can observe heterogeneous fields. More precisely, a detailed analysis (see [30]) shows that the mean value and the standard deviation of these fields increase with the load. At point B (see Fig. 8(a)), the mean value is very low and some grains are in contraction due to microstructural effects (grain size, crystallographic orientation, neighboring grains ...). On the opposite, the analysis of Fig. 8(b) shows that all the grains are in extension (with a mean value close to 1.45 %) and that highly strained grains are less numerous (with strain values greater that 3 %). Note that a few big grains with very low Schmid factors (see Fig. 1) also exhibit very low strain levels.

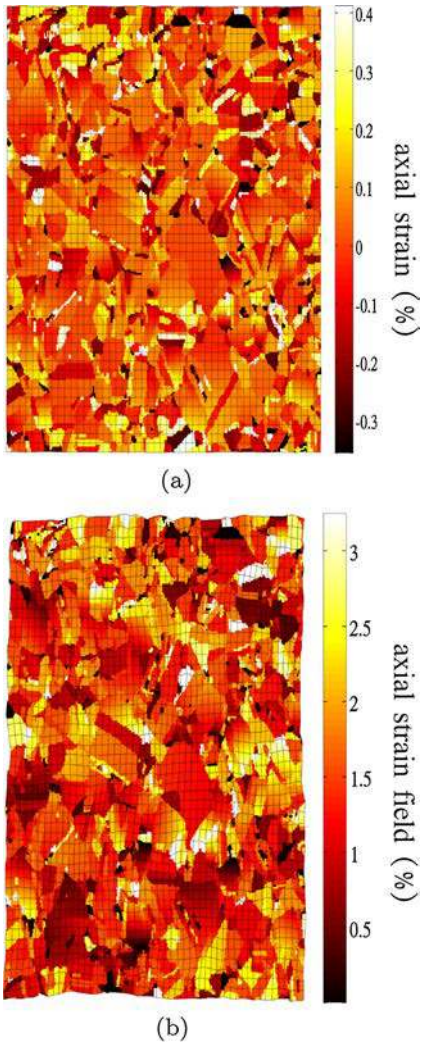

Fig. 8 Axial strain field (in %) in the 5 mm × 5 mm central area obtained from the projected displacement field by analytic differentiation: **a** at the point B and **b** in the plastic regime C (both points are reported on 7)

In Fig. 9(a), a relatively smooth heterogeneity is observed on the temperature field at point B; there is a competition between areas where temperature increases and others where temperature decreases, which conducts to the point (B) observed in Fig. 7. However, there is no real thermal localization phenomenon at this point compared to Fig. 9(b) where a thermal localization is clearly seen thanks to the conductive front from this localization area to the specimen boundaries. Note that this thermal localization is located within one of the highly deformed zones of Fig. 8, situated at the top and for which many grain boundary incompatibilities are also revealed in Figs. 3 and 4. Then, as strain localization at point C is not easy to detect by a pure kinematic analysis (see Fig. 8 where many highly strained zone are visible), the thermal localization appears clearly and is associated to a highly deformed area visible on the

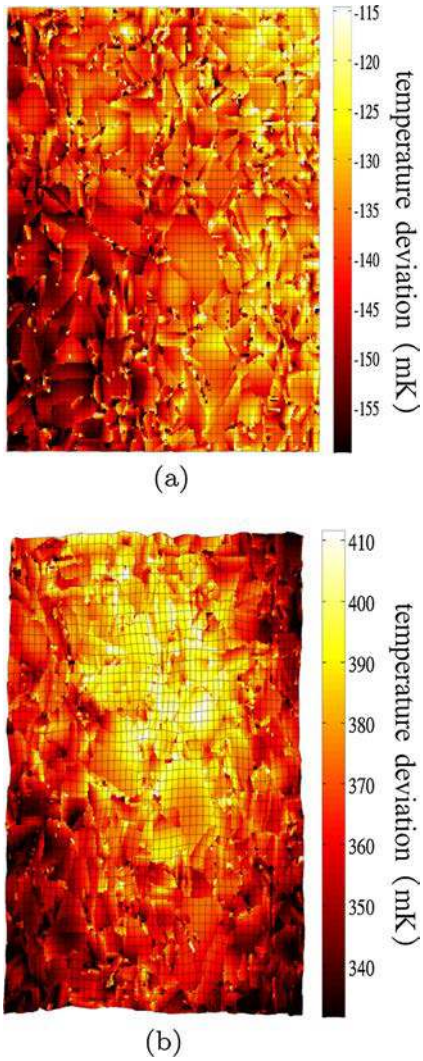

Fig. 9 Projected thermal field (in mK) in the 5 mm × 5 mm central area: (**a**) at the point B and (**b**) in the plastic regime C (both points are reported on equation (7))

micrography after the test (see Fig. 3). It is important to keep in mind that a strain field reflects a time cumulative history conducting to the final micrography presented in Fig. 3, whereas a temperature field reflects, in the present case, an instantaneous dissipative phenomenon. Note finally that thermal gradients between grains and inside grains can also be observed. This intragranular activity will now be analyzed.

Granular Analysis and Microplasticity

Temperature and Strain Fields in Grains

The grain presented in Fig. 10 is located in the left-side bottom part of the 5 mm x 5 mm central area (grain 1 in Fig. 1).

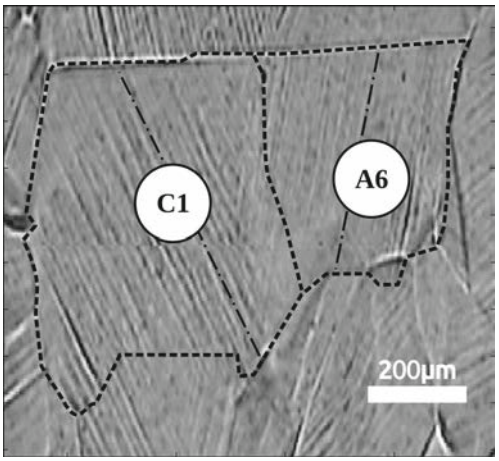

Fig. 10 Micrography of a particular zone, in the left bottom part of the 5 mm × 5mm central area. $C1$ and $A6$ indicate the activated slip systems

Its area is $0.16mm^2$ and, for the full-field analysis, it is composed of 16 cells measuring $100\mu m \times 100\mu m$ (related to the spatial resolutions). This grain has been selected because of its large size and also because it was far away from the more deformed area and not affected by the conductive front. The micrography analysis correlated with the EBSD data shows that two systems have been activated in this particular grain (see [28] for a complete description of crystallography basis): C_1 with a Schmid factor of 0.294 and A_6 with a Schmid factor of 0.269 (see Fig. 10). According to the Schmid theory, the C_1 system should be activated first because of a higher Schmid factor, followed by the A_6 system.

Figures 11(a) and (b), 12(a) and (b) respectively present intragranular shear strain ε_{12} and temperature fields at different levels of nominal stress, in the macroscopic elastic (a) or plastic (b) domains corresponding to points B and C in Fig. 7. As far as crystal plasticity is concerned, the main deformation mechanism is plastic slip on crystallographic planes. Therefore, only the shear strain ε_{12} is analyzed and, on the ε_{12} fields, thin black lines show the isovalues in order to underline the ε_{12} gradient orientation. A particular slip system is activated when these isovalues lines are coincident with the considered slip system orientation.

During the macroscopic elastic loading, Fig. 11(a) illustrates that the shear strain gradient is exactly oriented as the C_1 system slip marks. One could consequently affirm that, at this stress level which corresponds to a ratio $\sigma_{22}/R_{e\,0.2\,\%} \approx 0.5$, the C_1 system is activated. This is in line with the Schmid theory as the Schmid factor of this system is the highest one. Then, comparing Figs. 11(a) and (b), one can observe that ε_{12} exhibits a linear gradient that rotates during the test. In Fig. 11(b), which corresponds to a ratio

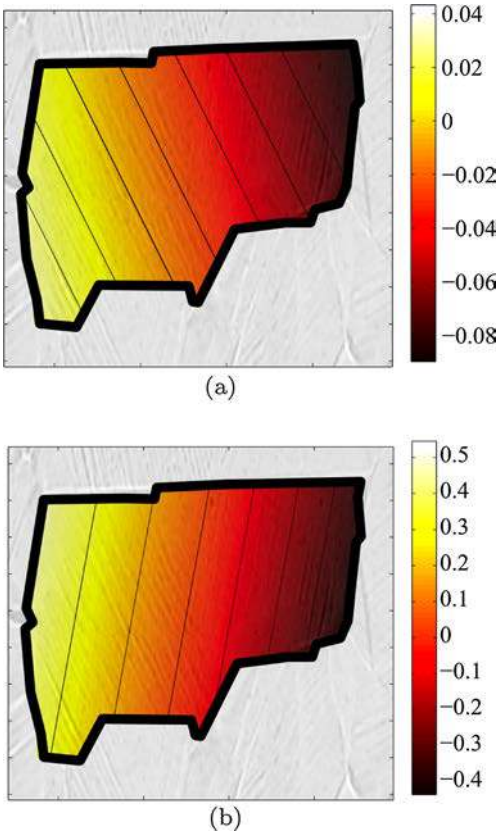

Fig. 11 Intragranular shear strain ε_{12} (in %): (**a**) at the point B and (**b**) in the plastic regime C (both points are reported on equation(7))

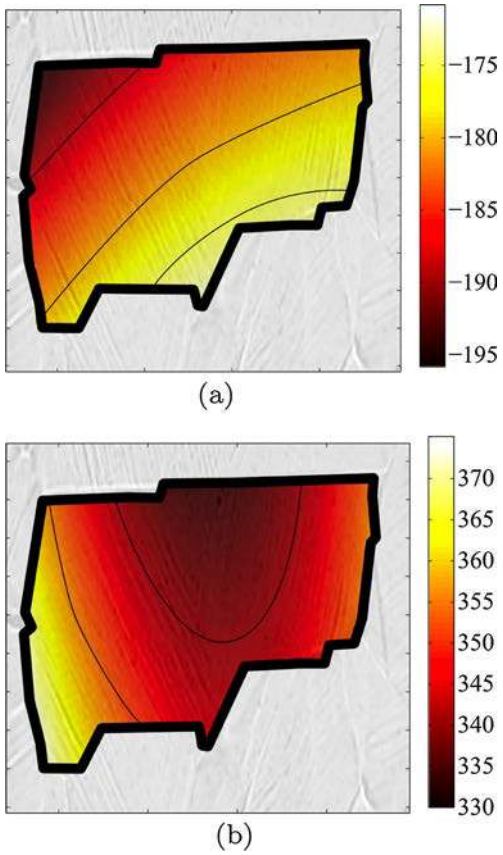

Fig. 12 Temperature variation (in mK): (**a**) at the point B and (**b**) in the plastic regime C (both points are reported on equation(7))

$\sigma_{22}/R_{e\,0.2\,\%} \approx 1.2$, this gradient coincides with the A_6 system slip marks and this is the case until the end of the test (not presented here). This rotation is observed close to the beginning of the macroscopic plastic response. One could therefore conclude that between these two instants, slip activation has changed from the C_1 system to the A_6 one. In Fig. 11(b), the shear strain orientation also shows that A_6 seems to be the only activated slip system during this last period, or the dominant one, since shear strain isovalues are oriented exactly like the A_6 system slip lines.

Figures 12(a) and (b) present thermal fields at points B and C. One can first observe that there is no direct link between shear strain and thermal fields as only thermal time gradients, rather than the current temperature, are representative of the dissipative sources linked to plastic strain. Thus, in order to understand how the intragranular thermal field could reflects the intragranular plastic activity, the time variation of the temperature is analyzed.

Figure 13 presents the temperature evolution of the grain highlighted in Fig. 10 during the first part of the loading, i.e. from 0 to 200 MPa. One observes successively the decrease and the increase of the mean temperature, and the nominal stress evolution. From point B to B' (106 to 191 MPa), the figure indicates that, with respect to the previous shear strain analysis, the C_1 slip system is activated. By using the Maximum Likelihood Method and a linear regression, it is then possible to identify the most likely instant when the mean thermal curve in the grain moves away from its linear drop. The green straight line corresponds to this identification and the deviation from linearity occurs at 106 MPa of nominal stress. With reference to the strain field analysis, this corresponds exactly to the beginning of the plastic activity of the C_1 slip system and also to the macroscopic thermal deviation from linearity point (see "Macroscopic Mean Values and Yield Stress Definition").

A similar method can be applied to each material point of the considered grain and Fig. 14 presents the spatial appearance of the deviation from linearity point as a function of the nominal stress.

This figure reveals that thermal deviation from linearity gradually appears within the grain. The first intragranular loss of thermal linearity initiates at 78 MPa of nominal stress within the C_1 domain and then propagates continuously through the C_1 domain in the left direction. Thus, it

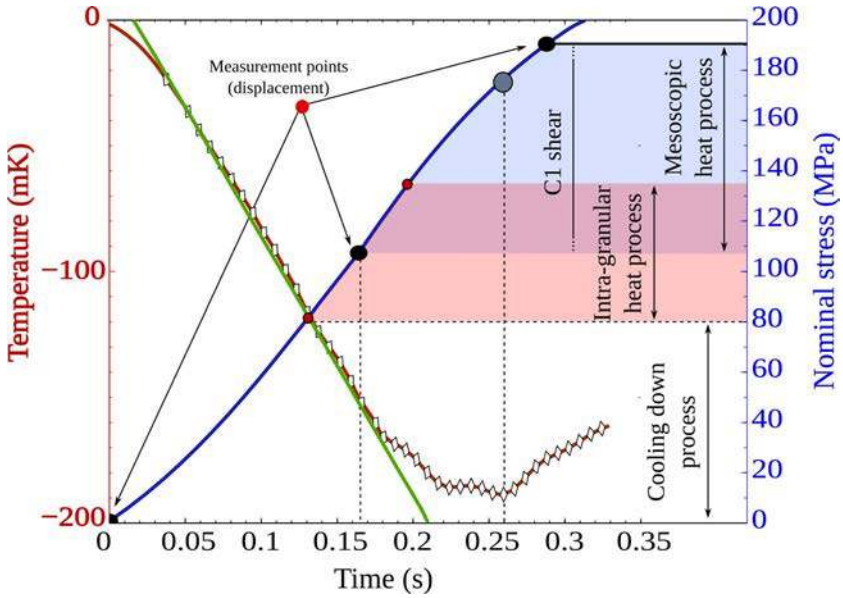

Fig. 13 Intragranular mean temperature (*red* - mK), linear regression with Maximum Likelihood Method (*green*) and nominal stress (*blue* - MPa) from the beginning to the end of macroscopic elasticity of the grain highlighted in Fig. 10

reveals that the first C_1 system activation has occurred earlier compared to the upper bound provided by the strain field analysis or the mean temperature in the grain.

Critical Resolved Shear Stress Determination

Let us now estimate the Critical Resolved Shear Stress (CRSS) related to the first activated system. One supposes that before the activation of the considered slip system, the local strain tensor in the considered grain is purely elastic. Let $\tilde{\mathbb{C}}$ be the local elastic fourth rank tensor. The local stress is then equal to:

$$\sigma = \tilde{\mathbb{C}} : \varepsilon \tag{6}$$

and the Resolved Shear Stress (shear stress acting on the considered slip system) is equal to

$$\tau^s = \sigma : \mathbb{M}^s \tag{7}$$

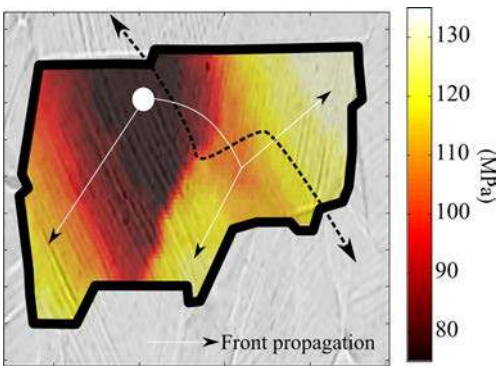

Fig. 14 Intragranular field of thermal "deviation from linearity" appearance expressed as a function of the nominal stress (in MPa)

where $\mathbb{M}^s$ is the Schmid tensor of the slip system s defined as $\mathbb{M}^s = \frac{1}{2}(\underline{n} \otimes \underline{v} + \underline{v} \otimes \underline{n})$. The vector $\underline{n}$ is the normal to the slip plane while $\underline{v}$ is the slip direction. At each loss of thermal linearity, it is possible to determine the local elastic strain tensor by considering the associated in-plane strain field and a plane stress assumption. Then, following the previous equations (6) and (7), the CRSS can be identified. The estimation of the Critical Resolved Shear Stress within the considered grain gives a value close to 32 MPa, for the material point where the first thermal deviation from linearity appears. This value is of the same order of magnitude as the one observed for a AISI 316L stainless steel single crystal [31] during a tensile test. This shows the consistency and accuracy of the proposed method. More analysis have been conducted on different grains, which leads to the same conclusions that the ones selected here. The comparison between grains and the statistical analysis will be dedicated to another article.

Intragranular Thermal Discontinuities

Figure 14 reveals additional elements. From 0 to 78 MPa of nominal stress, the entire grain is elastic and therefore, exhibits a uniform drop of temperature. From 78 MPa, the C_1 slip system is activated within the top part of the grain. Due to the thermoplastic coupling, a local dissipation occurs and the thermal front propagates continuously within the C_1 domain where the plastic behavior seems to be quite uniform.

While the C_1 domain dissipates, the neighboring domain A_6 is still elastic, thus the local temperature tends to linearly decrease due to the thermoelasticity. Therefore, the

thermal front shown in Fig. 14 does not propagate continuously from the C_1 to A_6 domain and Fig. 14 reveals a discontinuity at the interface between both domains, which is not a spatial discontinuity of temperature but a temporal one. When the thermoelasticity does not balance the dissipation anymore, the "deviation from linearity" wave front propagates through the grain. However, it is interesting to observe that the thermal front propagation towards the right part of the grain passes first through the area where very few slip-marks are visible in Fig. 10. All these observations evidence a complex connection between the intragranular thermal front propagation, the heterogeneity of the crystal plasticity activity and the surface topography evolution due to out-of plane displacement during the test. An important fact is that all the measurements have been done independently: strain field, temperature field, profilometry, slip bands density evaluation, ...

Conclusion

This paper is based on the experimental results of Bodelot et al. [22] who obtained coupled thermal and kinematic full-fields on a AISI 316L stainless steel polycrystal during a monotonic tensile loading. In order to perform intragranular thermomechanical analysis at the grain scale in this polycrystal, a crystallography-based technique for the projection of the temperature and displacement fields on a polynomial basis has been proposed. This projected data enable a microstructural analysis of the obtained fields. The application of this method also enables the study of the plastic activity within individual grains. This study shows the pertinence of the method since its intragranular coupled analysis of strain and temperature full-fields is consistent with the plastic slip activation. More particularly, this original method, which requires the simultaneous measurement of strain and temperature fields, makes the direct determination of a Critical Resolved Shear Stress on polycrystals possible, which has never been done before. The CRSS that has been determined is consistent with estimations obtained on single crystals by other authors. The results also show that microplasticity activates very early compared to the macroscopic one. This opens new perspectives for crystal plasticity models and more precisely their parameters identification as well as, for energy balance in polycrystals during monotonic and cyclic loadings.

Acknowledgments The authors would like to thank Patrick Villechaise at the Institut Pprime - UPR 3346 (ENSMA, Poitiers, France) for the EBSD analysis and fruitful discussions during this study.

The present research work has been supported by International Campus on Safety and Intermodality in Transportation (CISIT) the Nord-Pas-de-Calais Region, the European Community, the Ministry of Higher Education and Research, and the National Center for Scientific Research. The authors gratefully acknowledge the support of these institutions.

References

1. Sachs G (1928) Zur ableitung einer fliessbedingung. Z Ver Dtsch Ing 72:734–736
2. Schmid E (1924) Yield point of a crystals: critical shear stress law. In: Proc. 1st Int. Congr. Appl. Mech., Delft, Neetherland, pp 342
3. Taylor GI (1938) Plastic strains in metals. J Inst Metals 62:307
4. Cottrell A (1953) Dislocations and plastic flow in crystals. Clarendon Press, Oxford
5. Barrett C (1948) Structure of metals. McGraw-Hill Book Company Inc., New York
6. Boas W, Hargreaves M (1948) On the inhomogeneity of plastic deformation in the crystals of an aggregate. Proc Roy Soc A 193(1032):89–97
7. Michno M, Findley W (1976) An historical perspective of yield surface investigations for metals. Int J Non-Linear Mech 11(1):59–82
8. Farren WS, Taylor GI (1925) The heat developed during plastic extension of metals. Proc R Soc London Ser A, Containing Pap Math Phys Charact 107(743):422–451
9. Taylor GI, Quinney H (1934) The latent energy remaining in a metal after cold working. Proc R Soc Lond Ser A 143(849):307–326
10. Quinney H, Taylor GI (1937) The emission of the latent energy due to previous cold working when a metal is heated. Proc R Soc Lond Ser A Math Phys Sci 163(913):157–181
11. Lee H, Chen J (1991) Temperature effect induced by uniaxial tensile loading. J Mater Sci 26(21):5685–5692
12. Bever MB, Holt DL, Titchener AL (1973) The stored energy of cold work. Prog Mater Sci 17:5–177
13. Chrysochoos A, Maisonneuve O, Martin G, Caumon H, Chezeaux J (1989) Plastic and dissipated work and stored energy. Nucl Eng Des 114(3):323–333
14. Hodowany J, Ravichandran G, Rosakis A, Rosakis P (2000) Partition of plastic work into heat and stored energy in metals. Exp Mech 40:113–123
15. Macdougall D (2000) Determination of the plastic work converted to heat using radiometry. Exp Mech 40:298–306
16. Oliferuk W, Swiatnicki WA, Grabski MW (1993) Rate of energy storage and microstructure evolution during the tensile deformation of austenitic steel. Mater Sci Eng: A 161(1):55–63
17. Clarebrough LM, Hargreaves ME, West GW (1955) The release of energy during annealing of deformed metals. Proc R Soc A 232:252–270
18. Oliferuk W, Swiatnicki WA, Grabski MW (1995) Effect of the grain size on the rate of energy storage during the tensile deformation of an austenitic steel. Mater Sci Eng A 197(1):49–58
19. Badulescu C, Grédiac M, Haddadi H, Mathias JD, Balandraud X, Tran HS (2011) Applying the grid method and infrared thermography to investigate plastic deformation in aluminium multicrystal. Mech Mater 43(1):36–53
20. Saai A, Louche H, Tabourot L, Chang H (2010) Experimental and numerical study of the thermo-mechanical behavior of al bi-crystal in tension using full field measurements and micromechanical modeling. Mech Mater 42(3):275–292
21. Bodelot L, Charkaluk E, Sabatier L, Dufrénoy P (2011) Experimental study of heterogeneities in strain and temperature fields at the microstructural level of polycrystalline metals through

fully-coupled full-field measurements by digital image correlation and infrared thermography. Mech Mater 43(11):654–670
22. Bodelot L, Sabatier L, Charkaluk E, Dufrénoy P (2009) Experimental setup for fully coupled kinematic and thermal measurements at the microstructure scale of an aisi 316l steel. Mater Sci Eng A 501(1–2):52–60
23. Seghir R, Witz J, Charkaluk E, Dufrénoy P (2013b) Improvement of thermomechanical full-field analysis of metallic polycrystals by crystallographic informations. Meca Ind Accepted
24. Hild F, Roux S (2008) Correlli Q4: A software for "Finite-element" displacement field measurements by digital image correlation, internal report 269. Tech. rep., LMT Cachan, ENS Cachan, France
25. Pron H, Bissieux C (2004) Focal plane array infrared cameras as research tools. QIRT J 1(2):229–240
26. Berthel B (2007) Mesures thermographiques de champs de dissipation accompagnant la fatigue à grand nombre de cycles des aciers, PhD thesis, Thèse de doctorat de l'université de Montpellier II, Spécialité Mécanique, (in french), http://tel.archives-ouvertes.fr/tel-00410074/fr/
27. Seghir R, Witz J, Bodelot L, Charkaluk E, Dufrénoy P (2013a) Determination of microstructural lagrangian thermal field within polycrystals. QIRT journal Accepted
28. Kelly A, Knowles K (2012) Crystallography and crystal defects. Wiley
29. Nan C, Birringer R (1998) Determining the Kapitza resistance and the thermal conductivity of polycrystals: A simple model. Phys Rev B 57(14):8264–8268
30. Seghir R, Bodelot L, Charkaluk E, Dufrénoy P (2012) Numerical and experimental estimation of thermomechanical fields heterogeneity at the grain scale of 316L stainless steel. Comp Mat Sci 53(1):464–473
31. Feaugas X, Pilvin P (2009) A polycrystalline approach to the cyclic behaviour of fcc alloys: intra-granular heterogeneity. Adv Eng Mater 11(9):703–709